Optimal Excitation Angles Analysis Based on the SRM Quasi-Linear Normalized Model for Enhanced Overall Performance

Zhiyuan Chai, *Graduate Student Member, IEEE*, Yuefei Zuo, *Member, IEEE*, Shushu Zhu, Minjun Guan, Yao Sun, Wen Li, and Chuang Liu

***Abstract*—This article evaluates the comprehensive performance of switched reluctance motors (SRMs) using three key metrics: torque per ampere, average torque, and torque ripple, which cannot be simultaneously optimized at the same excitation angle. Traditional analytical methods for optimizing excitation angles (turn-ON and turn-OFF angles) focus solely on maximizing torque per ampere, resulting in complex formulas with limited general applicability. To overcome these limitations and ensure high-performance operation of the SRM across the entire torque-speed range, a generalized SRM quasi-linear normalized model is proposed, addressing the tradeoff between model accuracy and complexity. A multiobjective function is developed to coordinate the three performance metrics, and universal analytical formulas for optimal excitation angles are derived. The excitation angle controller requires only real-time detection of speed and reference current, enabling simple implementation. The precision and generality of the derived expressions are validated through comparisons with traditional finite-element methods using 12/8 three-phase and 8/6 four-phase SRMs. Simultaneously, considering the fringing effect and the back electromotive force in the low-inductance region, the current reference compensation in single pulse mode ensures that the target current peak is achieved. Finally, steady-state and dynamic experiments on a 12/8 three-phase prototype confirm the effectiveness of the optimal excitation angle formulas.**

***Index Terms*—Analytical formula, multiobjective function, optimal excitation angles, SRM quasi-linear normalized model (SRM-QLNM), switched reluctance motor (SRM).**

I. Introduction

SWITCHED reluctance motors (SRMs) are favored for their simple structure, robustness, and absence of permanent-magnet rotors, making them suitable for harsh environments and a wide range of speeds, particularly in automotive and aerospace starting/generating applications [1], [2], [3]. However, the inherent nonlinearity of their magnetic reluctance characteristics complicates accurate modeling and high-performance control, which depend on the optimization of excitation angles (turn-ON and turn-OFF angles). These technical limitations hinder the widespread adoption of SRMs. Consequently, researchers have focused on optimizing excitation angles to enhance torque per ampere for improve efficiency, increasing average torque for improved driving performance, and reducing torque ripple to minimize vibration and noise. However, achieving optimal performance for all three metrics simultaneously at a single excitation angle is impossible, necessitating multiobjective optimization for high-performance operation across the entire torque–speed range.

The operating state of the SRM is closely related to the phase currents, with the excitation angles determining the position of the phase current waveform relative to the phase inductance. This is a key factor influencing energy conversion and SRM performance, which can also be further improved by combining direct instantaneous torque control [4], [5], torque sharing function [6], [7], and vector control [8], [9], [10] to reduce torque ripple [11], [12]. Consequently, considerable research has been dedicated to optimizing the excitation angles, including lookup-table method [13], [14], [15], [16], [17], online optimization technique [18], [19], [20], [21], function analysis method [22], [23], [24], [25], [26], and their combinations [27], [28]. In [17], four scenarios were considered during the SRM design phase, combining average torque, torque per ampere, and torque ripple into single and multiobjective optimization problems to improve performance by optimizing the turn-ON and turn-OFF angles. In [13], [14], [15], and[16], multiobjective optimization techniques were employed to iterate the optimal turn-ON and turn-OFF angles, maximizing average torque, minimizing torque ripple, and achieving maximum efficiency, with the optimal excitation angle stored in a table for convenience. However, lookup-table methods rely on accurate motor models and extensive data processing. Multiobjective optimization using only online optimization and analytical methods is more challenging. Online optimization methods primarily target maximizing torque per ampere [18], [19], [20]. In [21], efficiency and torque ripple were used as objective functions, and genetic algorithms were applied for online optimization of the excitation angle.

Received 19 March 2025; revised 24 May 2025; accepted 4 July 2025. Date of publication 10 July 2025; date of current version 27 August 2025. This work was supported in part by the National Natural Science Foundation of China under Project 52277054, in part by Postgraduate Research and Practice Innovation Program of Jiangsu Province under Grant KYCX24-0577, in part by Funding for Outstanding Doctoral Dissertation in NUAA under Grant BCXJ25-08, and in part by Interdisciplinary Innovation Fund for Doctoral Students of Nanjing University of Aeronautics and Astronautics under Grant KXKCXJJ202401. Recommended for publication by Associate Editor F. W. Fuchs. *(Corresponding author: Chuang Liu.)*

The authors are with the Electrical Engineering, College of Automation, Nanjing University of Aeronautics and Astronautics, Nanjing 211106, China (e-mail: chai199901@nuaa.edu.cn; yuefei.zuo@ieee.org; s.zhu@nuaa.edu.cn; guanmj@jit.edu.cn; sunyao@nuaa.edu.cn; nuaalw@nuaa.edu.cn; lc@nuaa.
edu.cn).

Color versions of one or more figures in this article are available at https://doi.org/10.1109/TPEL.2025.3587294.

Digital Object Identifier 10.1109/TPEL.2025.3587294

However, this approach requires obtaining the corresponding coefficients before applying the genetic algorithm, and its computational accuracy decreases at higher speeds. While online optimization avoids control errors caused by inaccurate models or parameters, the algorithm is complex to design and has poor dynamic response.

Compared to other methods, the function analysis method based on the SRM motor model offers advantages in solving efficiency and fast dynamic response, making it the preferred choice for excitation angle optimization. In [24], an optimal turn-ON angle analytical formula was proposed for the SRM high-speed single pulse mode (SPM) operation, which is related to the geometric parameters of the motor and maximizes torque. To maximize efficiency, the authors in [22] and [27] proposed an analytical method to optimize the turn-ON angle based on an SRM linear model with a constant low-inductance region, ensuring that phase current reaches the reference current exactly when the stator and rotor poles begin to overlap. However, the fringing effect in the actual low-inductance region and the influence of back electromotive force (back EMF) result in low accuracy. In [23] and [29], nonlinear modeling of the low-inductance region was performed, considering back EMF effects, leading to a more accurate analytical formula for the optimal turn-ON angle. However, the analysis from a phase current perspective is quite complex. Simultaneously, optimizing the turn-OFF angle ensures that phase current drops to zero before the motor enters the negative torque region, but requires offline measurement of coefficients under current chopping mode (CCM). In [25], an in-depth analysis from the flux linkage perspective provided a more accurate and structurally simpler optimal turn-ON angle formula, although it requires detailed parameters for nonlinear inductance. In [27] and [28], the lookup-table method was combined to optimize both efficiency and torque ripple. In [22] and [26], the optimal excitation angle was derived based on the optimal magnetic flux linkage from an SRM linear model, optimizing both efficiency and torque ripple through multiobjective optimization; however, offline parameter determination complicates implementation.

The variation in phase numbers and stator/rotor pole pairs complicates SRM modeling and control, limiting its widespread adoption. Due to these constraints, existing optimal excitation angle formulas lack general applicability. Most function analysis methods focus primarily on maximizing torque per ampere while overlooking average torque and torque ripple optimization. The main contributions of this article are summarized as follows:

1) To balance model accuracy and complexity while accounting for saturation effects, the SRM quasi-linear normalized model (SRM-QLNM) is proposed by integrating the SRM linear normalized model [30] and the SRM quasi-linear model (SRM-QLM) [31]. Parameter normalization simplifies analytical complexity and unifies models across different SRM structures, enhancing the universality of control parameters.
2) The optimal turn-ON and turn-OFF angles are redefined to optimize the average torque, torque ripple, and torque per ampere simultaneously. Based on SRM-QLNM, analytical formulas for optimal excitation angles are derived, ensuring high-performance operation in both CCM and SPM.
3) To address nonlinearities in the low-inductance region, a compensation method for current reference values in closed-loop control under SPM is proposed, ensuring that the phase current peaks reach the reference values.

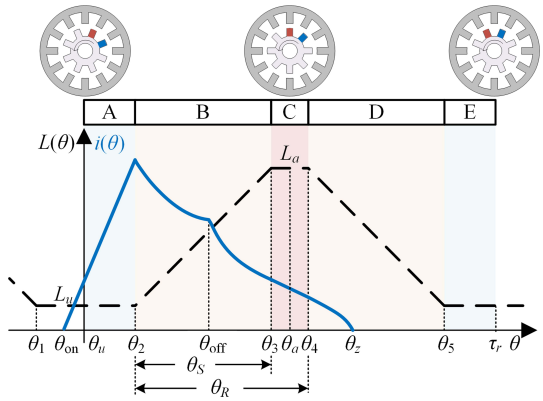

Fig. 1. Phase current and inductance waveforms of the SRM-QLM.

The rest of this article is organized as follows. In Section II, the SRG-QLNM is established and its accuracy is verified by comparison with the nonlinear model. In Section III, the optimal excitation angles are derived based on SRM-QLNM and validated for accuracy and generality by comparison with the finite-element traversal results. In Section IV, experiments are conducted to confirm the effectiveness and generality of the SRG-QLNM and the analytical formulas for optimal excitation angles. Finally, Section V concludes this article.

II. Establishment of the SRM-QLNM

A. Traditional SRM-QLM

In practical SRM operation, the phase inductance $L(\theta)$ is influenced by magnetic saturation. To avoid complex calculations while maintaining reasonable accuracy, the SRM-QLM is commonly used to approximate the saturation effects in the magnetic circuit. As shown in Fig. 1, the phase current and phase inductance waveforms for the SRM-QLM are plotted, with the rotor position θ on the horizontal axis. L_u and L_a represent the phase inductance values at the unaligned position θ_u and aligned position θ_a, respectively. Using θ_u as the zero position, the characteristic positions are determined based on the motor's structural parameters, namely the stator pole arc angle θ_S and rotor pole arc angle θ_R. The analytical relationship is given by

$$\begin{cases} \theta_2 = (\tau_r - \theta_S - \theta_R)/2 \\ \theta_3 = \theta_2 + \theta_S \\ \theta_4 = \theta_2 + \theta_R \\ \theta_5 = \tau_r - \theta_2 \\ \tau_r = 360/N_r \end{cases} \tag{1}$$

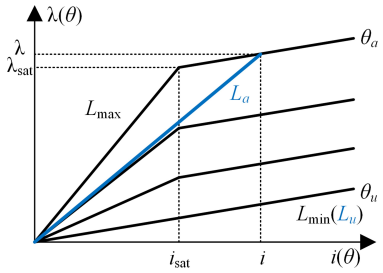

Fig. 2. Piecewise linearized magnetization curve of the SRM-QLM.

where τ_r represents the rotor pole pitch, and N_r is the number of rotor poles.

By performing a piecewise linear approximation of the magnetization curve of the SRM nonlinear model [32], the magnetization curve of the SRM-QLM is obtained, as shown in Fig. 2, where i_{sat} is the saturation current, which represents the boundary between the unsaturated and saturated regions of the flux linkage. The flux linkage at θ_a corresponding to i_{sat} is denoted as λ_{sat}. When the phase current $i(\theta) \le i_{\text{sat}}$, the magnetic circuit is unsaturated, and its slope represents the maximum inductance $L_{\max}$. When $i(\theta) > i_{\text{sat}}$, the magnetic circuit is saturated, and it can be approximated as being parallel to the minimum inductance $L_{\min}$. The formulas for $L_{\max}$ and $L_{\min}$ are derived as

$$\begin{cases} L_{\max} = \lambda_{\text{sat}}/i_{\text{sat}} \\ L_{\min} = (\lambda - \lambda_{\text{sat}})/(i - i_{\text{sat}}). \end{cases} \tag{2}$$

Due to the unsaturated condition at the unaligned position, $L_u = L_{\min}$, L_a is affected by core saturation and depends on the phase current value. From (2), L_a can be derived as

$$L_a = \lambda/i = \begin{cases} L_{\max}, & i \le i_{\text{sat}} \\ L_{\min} + (L_{\max} - L_{\min}) i_{\text{sat}}/i, & i > i_{\text{sat}}. \end{cases} \tag{3}$$

Therefore, the piecewise analytical formula of $L(\theta)$ in each region shown in Fig. 1 can be derived as (4), where the slope K in the inductance rising region can be expressed as (5).

$$L(\theta) = \begin{cases} L_u, & \text{A} \\ L_u + K(\theta - \theta_2), & \text{B} \\ L_a, & \text{C} \\ L_a - K(\theta - \theta_4), & \text{D} \\ L_u, & \text{E} \end{cases} \tag{4}$$

$$K = \frac{L_a - L_u}{\theta_S}. \tag{5}$$

According to the Faraday's law of electromagnetic induction, the relationship between the phase flux linkage $\lambda(\theta)$, the dc bus voltage U_{dc}, and the rotor electrical angular velocity ω_r is given by

$$\lambda(\theta) = \frac{U_{dc}}{\omega_r}\Delta\theta = \begin{cases} \frac{U_{dc}}{\omega_r}(\theta - \theta_{\text{on}}), & \theta \in [\theta_{\text{on}}, \theta_{\text{off}}] \\ \frac{U_{dc}}{\omega_r}(\theta_z - \theta), & \theta \in [\theta_{\text{off}}, \theta_z]. \end{cases} \tag{6}$$

TABLE I
CHARACTERISTIC PARAMETERS OF THE 12/8 THREE-PHASE SRM

Parameters	Value
Stator pole arc angle θ_S (°)	15.5
Rotor pole arc angle θ_R (°)	19
The maximum inductance $L_{\max}$ (μH)	258
The minimum inductance $L_{\min}$ (μH)	32
Saturation current i_{sat} (A)	125

Based on (4) and (6), the piecewise analytical formula for the phase current $i(\theta)$ under the SRM-QLM can be derived as

$$i(\theta) = \frac{\lambda(\theta)}{L(\theta)} = \begin{cases} \frac{U_{dc}(\theta - \theta_{\text{on}})}{\omega_r L_u}, & \theta \in [\theta_{\text{on}}, \theta_2] \\ \frac{U_{dc}(\theta - \theta_{\text{on}})}{\omega_r[L_u + K(\theta - \theta_2)]}, & \theta \in [\theta_2, \theta_{\text{off}}] \\ \frac{U_{dc}(\theta_z - \theta)}{\omega_r[L_u + K(\theta - \theta_2)]}, & \theta \in [\theta_{\text{off}}, \theta_3] \\ \frac{U_{dc}(\theta_z - \theta)}{\omega_r L_a}, & \theta \in [\theta_3, \theta_4] \\ \frac{U_{dc}(\theta_z - \theta)}{\omega_r[L_a - K(\theta - \theta_4)]}, & \theta \in [\theta_4, \theta_z]. \end{cases} \tag{7}$$

B. SRM Quasi-Linear Normalized Model (SRM-QLNM)

To simplify the SRM-QLM and create a universal SRM mathematical model, the parameters in the SRM-QLM are normalized, resulting in the SRM-QLNM. This approach eliminates the need for unit conversions between parameters, reducing analytical complexity. In addition, the control parameter formulas derived from this model can be directly applied to SRMs with different structural parameters, ensuring strong universality. Table I lists the key characteristic parameters required for establishing the SRM-QLNM. Taking the 12/8 three-phase SRM as an example, these include the stator and rotor pole arc angles θ_S and θ_R, the maximum inductance $L_{\max}$, the minimum inductance $L_{\min}$, and the saturation current i_{sat}.

Four original basic values are defined: the angle basic value θ_N, the voltage basic value U_N, the speed basic value ω_N, and the inductance basic value L_N, as (8). The definitions of other variable basic values must satisfy the following two conditions:

1) the basic values should have a magnitude of 1;
2) the mathematical relationship between the actual values should be extendable to the basic values

$$\begin{cases} \theta_N = \theta_s \\ U_N = U_{\text{dc}} \\ \omega_N = \omega_r \\ L_N = L_{\max} - L_{\min}. \end{cases} \tag{8}$$

Therefore, based on (5), (6), and (7), the basic values for the flux linkage λ_N, the current I_N, and the inductance rising region slope K_N can be derived as (9).

$$\begin{cases} \lambda_N = U_N \theta_N/\omega_N \\ I_N = \lambda_N/L_N = U_N\theta_N/(\omega_N L_N) \\ K_N = L_N/\theta_N. \end{cases} \tag{9}$$

Therefore, the normalized values of various parameters can be derived, including the normalized angle α, the normalized aligned inductance b, the normalized unaligned inductance b',

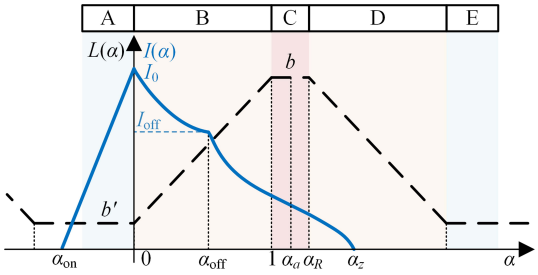

Fig. 3. Phase current and inductance waveforms of the SRM-QLNM.

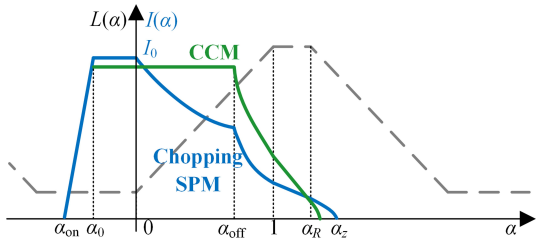

Fig. 4. Typical phase current waveforms of the SRM.

and the normalized current $I(\alpha)$ as (10), as well as the normalized inductance rising region slope K^* as (11).

$$\begin{cases} \alpha = \theta/\theta_N \\ b = L_a/L_N \\ b' = L_u/L_N \\ I(\alpha) = i(\theta)/i_N \end{cases} \tag{10}$$

$$K^* = \frac{(L_a - L_u)/\theta_S}{K_N} = b - b'. \tag{11}$$

Based on Fig. 1, since the phase current of the SRM is primarily distributed in the inductance rising region $[\theta_2, \theta_3]$, the normalized phase current formula is simplified by shifting the coordinate origin to θ_2, i.e., $\theta_2 = 0$, as shown in Fig. 3. During generation operation, the phase current is primarily distributed in the inductance decrease region $[\theta_4, \theta_5]$. Therefore, to simplify the normalized phase current formula, the coordinate origin is shifted to θ_4 [30]. The horizontal axis represents the rotor position normalized value α, and the normalized phase current at the origin is I_0.

Based on the Faraday's law of electromagnetic induction, and neglecting the voltage drop across power devices and the winding resistance, the voltage balance equation is derived as

$$U(\theta) = d\lambda(\theta)/dt = \omega_r d\left[i(\theta)L(\theta)\right]/d\theta. \tag{12}$$

By normalizing the parameters in (12), the voltage balance equation under SRM-QLNM can be obtained as

$$U(\alpha)d\alpha = d\left[\lambda(I,\alpha)\right] = d\left[I(\alpha)L(\alpha)\right] \tag{13}$$

where $L(\alpha)$ is the normalized phase voltage, $\lambda(I,\alpha)$ is the normalized flux linkage of the phase winding, and $L(\alpha)$ is the normalized phase inductance.

Based on (4), the piecewise analytical formula of $L(\alpha)$ can be represented as

$$L(\alpha) = \begin{cases} b', & \text{A} \\ b' + (b-b')\alpha, & \text{B} \\ b, & \text{C} \\ b - (b-b')(\alpha - \alpha_R), & \text{D} \\ b', & \text{E}. \end{cases} \tag{14}$$

Substituting (14) into (13) and integrating both sides with respect to α, the piecewise analytical formula of $I(\alpha)$ is derived as

$$I(\alpha) = \begin{cases} \frac{\alpha - \alpha_{on}}{b'}, & \alpha \in [\alpha_{on}, 0] \\ \frac{\alpha - \alpha_{on}}{b' + (b-b')\alpha}, & \alpha \in [0, \alpha_{off}] \\ \frac{\alpha_z - \alpha}{b' + (b-b')\alpha}, & \alpha \in [\alpha_{off}, 1] \\ \frac{\alpha_z - \alpha}{b}, & \alpha \in [1, \alpha_R] \\ \frac{\alpha_z - \alpha}{b - (b-b')(\alpha - \alpha_R)}, & \alpha \in [\alpha_R, \alpha_z]. \end{cases} \tag{15}$$

The SRM's operating modes can be classified based on the phase current waveform into the nonchopping SPM (see Fig. 3), chopping SPM (blue line in Fig. 4), and CCM (green line in Fig. 4). Since the derivation of (15) does not consider current chopping, it is only valid for the nonchopping SPM. The normalized value of the reference current i_{ref} is defined as I_0, which increases with the SRM's speed and load, thereby allowing for the assessment of the SRM's operating conditions.

As shown in Fig. 4, when the SRM operates in CCM, the normalized phase current in the interval $[\alpha_0, \alpha_{off}]$ is I_0. When operating in the chopping SPM, the normalized phase current in the interval $[\alpha_0, 0]$ is I_0. Here, α_0 is the normalized rotor position where the phase current first reaches I_0. Based on (15), α_0 can be derived as

$$\alpha_0 = I_0 b' + \alpha_{on}. \tag{16}$$

Therefore, the analytical relationship between $I(\alpha)$ and I_0 can be derived, ensuring that $I(\alpha)$ is valid for all three operating modes. In SPM, the normalized phase current formula in the interval $\alpha \in [0, \alpha_{off}]$ can be obtained by integrating both sides of (13) with respect to α, as shown in (17). The final analytical relationship between $I(\alpha)$ and I_0 is derived as (18).

$$\alpha\big|_0^\alpha = I(\alpha)\left[b' + (b-b')\alpha\right]\big|_0^\alpha \tag{17}$$

$$I(a) = \frac{\alpha + I_0 b'}{b' + (b-b')\alpha}. \tag{18}$$

The SRM's operating mode can be determined by the sign of the derivative of $I(\alpha)$ with respect to α in (18). When I_0 satisfies the condition in (19), $I(\alpha)$ will decrease, corresponding to SPM. Conversely, it corresponds to CCM.

$$\frac{dI(\alpha)}{d\alpha} = \frac{b' - (b-b')I_0 b'}{\left[b' + (b-b')\alpha\right]^2} < 0 \Rightarrow I_0 > \frac{1}{b-b'}. \tag{19}$$

From (15), it can be seen that $I(\alpha)$ depends on α_z during the demagnetization stage $[\alpha_{off}, \alpha_z]$. By combining (15) and (18)

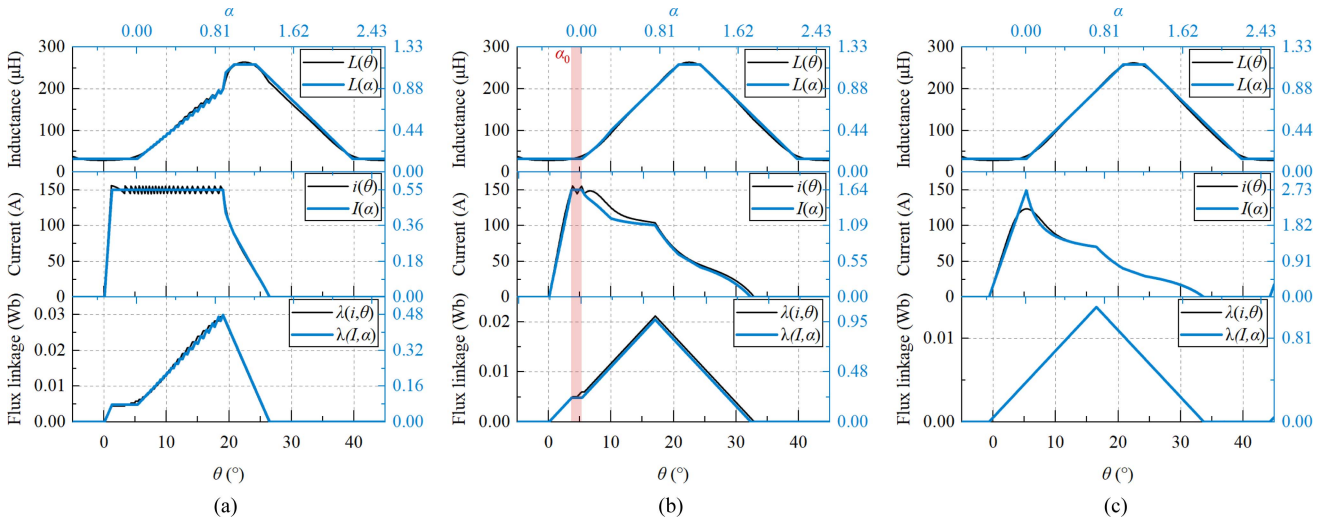

Fig. 5. Comparison between the SRM-QLNM (upper and right axes) and the nonlinear model (lower and left axes). (a) CCM. (b) Chopping SPM.(c) Nonchopping SPM.

TABLE II
ROTATIONAL SPEEDS AND EXCITATION ANGLES CORRESPONDING TO EACH OPERATING CONDITION

Parameters	CCM	chopping SPM	nonchopping SPM
n/(r/min)	2000	6000	10000
$(\theta_{\text{on}}, \theta_{\text{off}})$	(0°,19°)	(0°,17°)	(–0.75°,16.5°)

with the normalized phase current I_{off} at α_{off}, the analytical relationship between α_z and I_0 can be obtained as

$$\alpha_z = \begin{cases} \alpha_{\text{off}} + I_0\left[b' + (b-b')\alpha_{\text{off}}\right], & \text{CCM} \\ 2\alpha_{\text{off}} + I_o b', & \text{SPM.} \end{cases} \tag{20}$$

C. Validation of SRM-QLNM Accuracy

To validate the accuracy of the derived SRM-QLNM, comparisons between SRM-QLNM and the nonlinear model were conducted under CCM, chopping SPM, and nonchopping SPM modes for inductance, current, and flux linkage waveforms of the phase winding, as shown in Fig. 5. The reference current was set to 150 A with a hysteresis width of ±5 A. The speeds n and excitation angles $(\theta_{\text{on}}, \theta_{\text{off}})$ corresponding to the three operating modes are listed in Table II.

According to (13), $\lambda(I,\alpha)$ can be expressed in (21). For the nonchopping segment within one electrical period, $\lambda(I,\alpha)$ can also be described by (22).

$$\lambda(I,\alpha) = L(\alpha)I(\alpha) \tag{21}$$

$$\lambda(I,\alpha) = \begin{cases} \alpha - \alpha_{\text{on}}, & \alpha \in [\alpha_{\text{on}}, \alpha_{\text{off}}] \\ \alpha_z - \alpha, & \alpha \in [\alpha_{\text{off}}, \alpha_z]. \end{cases} \tag{22}$$

As shown in Fig. 5(a) and (c), the SRM-QLNM exhibits high consistency with the nonlinear model under the CCM and nonchopping SPM. However, in the chopping SPM depicted in Fig. 5(b), relatively large discrepancies are observed between the SRM-QLNM and the nonlinear model in terms of phase current and flux linkage. The red-shaded area highlights that within the interval $[\alpha_0, 0]$, both $L(\alpha)$ and $I(\alpha)$ remain constant in the SRM-QLNM, resulting in a steady $\lambda(I,\alpha)$. In contrast, due to chopping effects, $\lambda(i,\theta)$ continues to increase during this interval. For $\alpha > 0$, when the phase current no longer undergoes chopping, the slopes of $\lambda(I,\alpha)$ during its increase and decrease remain unchanged as (22), consistently falling below $\lambda(i,\theta)$. Consequently, the corresponding normalized phase current $I(\alpha)$ and α_z also exhibit smaller values.

III. OPTIMAL EXCITATION ANGLE ANALYSIS BASED ON SRM-QLNM

Under the condition that the phase current reaches I_0, the turn-ON angle θ_{on} affects the phase current in the interval $\alpha < 0$, while the turn-OFF angle θ_{off} influences the phase current in $\alpha > 0$. Therefore, the optimization processes for θ_{on} and θ_{off} are mutually independent.

A. Optimal Turn-OFF Angle Analysis

The turn-OFF ratio α_{Kom} is defined as follows, which describes the ratio of the demagnetization time after the aligned position normalized value α_a to the total demagnetization time:

$$\begin{cases} \alpha_{\text{Kom}} = (\alpha_z - \alpha_a)/(\alpha_z - \alpha_{\text{off}}) \\ \alpha_a = (1 + \alpha_R)/2. \end{cases} \tag{23}$$

By substituting (20) into (23), the analytical relationships between α_{off} and α_{Kom} under CCM and SPM modes can be derived as (24). α_{off} increases with α_{Kom}. To determine the optimal turn-OFF angle normalized value $\alpha_{\text{off\_opt}}$, the optimal turn-OFF ratio $\alpha_{\text{Kom\_opt}}$ must be identified.

$$\alpha_{\text{off}} = \begin{cases} \frac{\alpha_a - I_0 b'(1-\alpha_{\text{Kom}})}{1+I_0(b-b')(1-\alpha_{\text{Kom}})}, & \text{CCM} \\ \frac{\alpha_a - I_0 b'(1-\alpha_{\text{Kom}})}{2-\alpha_{\text{Kom}}}, & \text{SPM.} \end{cases} \tag{24}$$

To balance three key SRM performance metrics: torque per ampere T/I, average torque T_{avg}, and torque ripple ΔT [9], a multiobjective function F_{obj} is defined as (25). T/I is of great importance under all operating conditions. The influence of ΔT on the motor is more obvious in CCM, while it is less significant in SPM. Under SPM, increasing T_{avg} can improve the utilization rate of the bus voltage. According to the optimization focus, k_1=0.5, k_2=0.2, k_3=0.3 have been used in CCM, while k_1=0.5, k_2=0.4, k_3=0.1 have been used in SPM.

$$F_{\text{obj}} = k_1 \frac{T/I - (T/I)_{\min}}{(T/I)_{\max} - (T/I)_{\min}} + k_2 \frac{T_{\arg} - (T_{\arg})_{\min}}{(T_{\arg})_{\max} - (T_{\arg})_{\min}} + k_3 \frac{(\Delta T)_{\max} - \Delta T}{(\Delta T)_{\max} - (\Delta T)_{\min}}. \tag{25}$$

To ensure that the phase current reaches I_0, θ_{on} is determined by selecting $\alpha_0 = -0.1$ according to (16). The impact of different α_{Kom} values on three performance metrics under the same operating condition (i.e., I_0) is analyzed. The normalized torque per ampere $(T/I)_{\text{norm}}$, average torque $(T_{\text{avg}})_{\text{norm}}$, and torque ripple $(\Delta T)_{\text{norm}}$ are defined as follows:

$$\begin{cases} (T/I)_{\text{norm}} = (T/I)\,/\,(T/I)_{\max} \\ (T_{\text{avg}})_{\text{norm}} = T_{\text{avg}}/\,(T_{\text{avg}})_{\max} \\ (\Delta T)_{\text{norm}} = (\Delta T)_{\min}\,/\Delta T \end{cases} \tag{26}$$

where $(T/I)_{\max}$ represents the maximum torque per ampere at the same I_0, while $(T_{\text{avg}})_{\max}$ denotes the maximum average torque, and $(\Delta T)_{\min}$ indicates the minimum torque ripple.

A comprehensive simulation of α_{off} was conducted using a 12/8 three-phase SRM under various operating conditions, iterating through I_0 and α_{Kom} to obtain the corresponding $(T/I)_{\text{norm}}$, $(T_{\text{avg}})_{\text{norm}}$, $(\Delta T)_{\text{norm}}$, and F_{obj}, as illustrated in Fig. 6. It can be observed that for all values of I_0, the maximum value of $(T_{\text{avg}})_{\text{norm}}$ occurs around $\alpha_{\text{Kom}} = 0.65$, which aligns with the numerically derived result in [33]. When $I_0 < 1$, reducing α_{Kom} enhances both $(T/I)_{\text{norm}}$ and $(\Delta T)_{\text{norm}}$, which is also reflected in the behavior of the multiobjective function F_{obj}. For $I_0 > 1$, a decrease in α_{Kom} leads to an improvement in $(T/I)_{\text{norm}}$.

In order to analyze the influence of different coefficients k_1, k_2, and k_3 on the results of F_{obj}, the influences of α_{Kom} on T/I, T_{avg}, and ΔT under different I_0 were respectively obtained, as shown in Fig. 6. It can be found that these three performance metrics all have good results when $\alpha_{\text{Kom}} = 0.65$. Therefore, $\alpha_{\text{Kom\_opt}} = 0.65$ is defined based on the principle of maximizing F_{obj}.

In summary, based on the SRM-QLNM, $\alpha_{\text{off\_opt}}$ in both CCM and SPM is solely dependent on I_0 as (27), and remains continuous at the boundary between the two modes.

$$\alpha_{\text{off\_opt}} = \begin{cases} \frac{\alpha_a - 0.35 I_0 b'}{1 + 0.35 I_0 (b - b')}, & I_0 \le \frac{1}{b - b'} \\ \frac{\alpha_a - 0.35 I_0 b'}{1.35}, & I_0 > \frac{1}{b - b'}. \end{cases} \tag{27}$$

B. Optimal Turn-ON Angle Analysis

As shown in Fig. 7, the inductance, current, and torque waveforms of each phase under CCM ($n = 3000$ r/min, $i_{\text{ref}} = 150$ A) are presented. From the shaded region, it can be observed

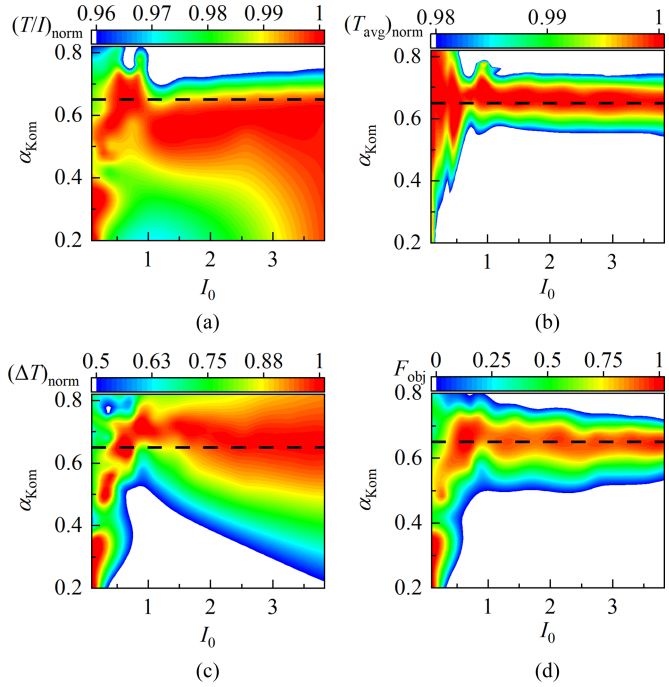

Fig. 6. Impact of different I_0 and α_{Kom} on performance metrics. (a) T/I_{norm}. (b) $T_{\text{avg\_norm}}$. (c) ΔT_{norm}. (d) F_{obj}.

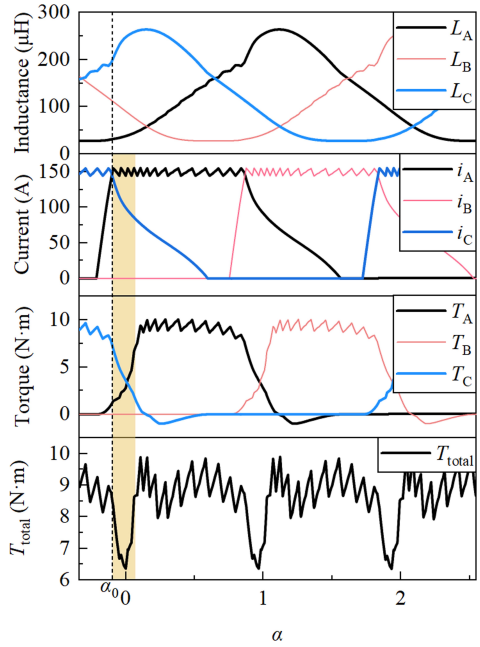

Fig. 7. Inductance, current, and torque waveforms under CCM operation.

that the torque of the incoming phase (Phase A) increases rapidly only when $\alpha > 0$, resulting in the minimum value of T_{total} occurring near $\alpha = 0$. According to (16), α_0 determines the value of α_{on}. To minimize torque ripple, it is required that $\alpha_0 < 0$. As α_0 decreases, T_{avg} increases while T/I decreases.

The multiobjective function values F_{obj} for different values of α_0 within the interval $[-0.14, 0]$ were evaluated under various operating conditions (i.e., I_0), as shown in Fig. 8. It is observed

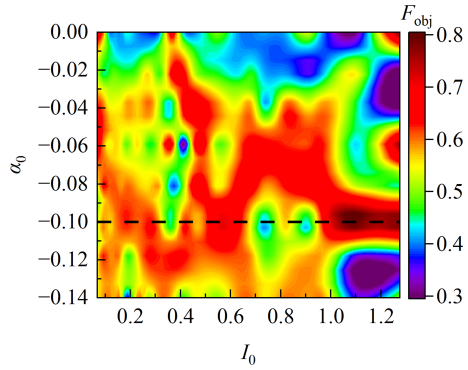

Fig. 8. Impact of different I_0 and α_0 on F_{obj} under CCM operation.

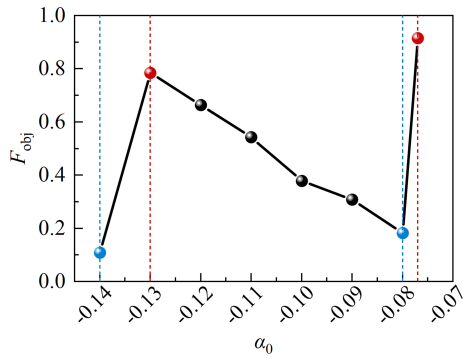

Fig. 9. Influence of α_0 on F_{obj} under SPM operation.

that the α_0 value that maximizes F_{obj} does not stabilize at a fixed value across different I_0. This is due to the uncertainty in current amplitude at the turn- OFF moment under current chopping control, which further influences the phase current amplitude in the demagnetization interval. The wider the loop, the more significant this uncertainty becomes. The choice of $\alpha_0 = -0.1$ is a compromise, considering the different operating conditions. Consequently, the analytical formula for the optimal normalized turn- ON angle α_{on_opt} under CCM is derived as

$$\alpha_{on\_opt} = -0.1 - I_0 b'. \tag{28}$$

As shown in Fig. 9, the SRM operates in SPM mode ($n = 8000$, r/min, and $i_{ref} = 150$, A), with different values of α_0 yielding corresponding F_{obj}. Two maxima are observed at $\alpha_0 = -0.077$ and $\alpha_0 = -0.13$, while two minima are located at $\alpha_0 = -0.08$ and $\alpha_0 = -0.14$. The phase current waveforms corresponding to these four specific values of α_0 are extracted and presented in Fig. 10. It can be observed that the emergence of these extrema is due to the differing phase current magnitudes at the turning point of phase inductance (θ_2). This current chopping inherently introduces uncertainty, making it difficult to determine the optimal α_0. Therefore, maintaining nonchopping current ensures that F_{obj} is maximized, which not only enhances the overall performance of the SRM but also reduces switching losses.

Based on (20) and (27), the analytical values of α_{off} and α_z are independent of α_0 and thus remain constant. According to

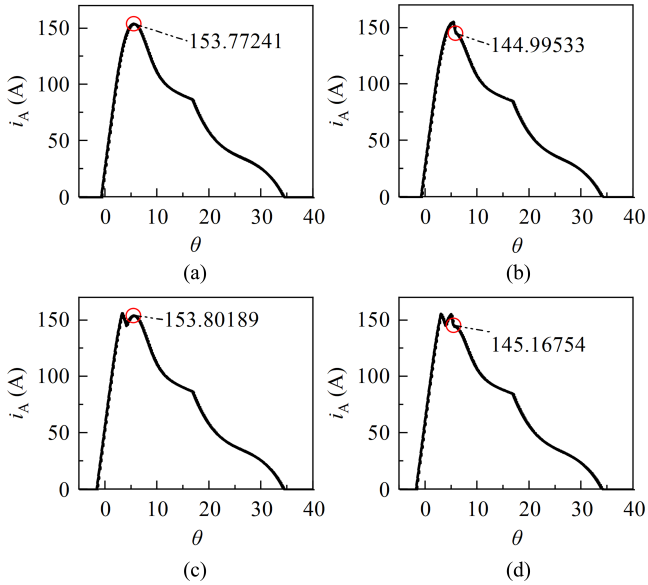

Fig. 10. Phase current waveforms corresponding to the four special values of α_0. (a) $\alpha_0 = -0.077$. (b) $\alpha_0 = -0.08$. (c) $\alpha_0 = -0.13$. (d) $\alpha_0 = -0.14$.

Fig. 5(b), when $\alpha_0 < 0$, the actual value of α_z obtained from the sampled phase current will be larger, resulting in an increased actual α_{Kom} as (23). Therefore, setting $\alpha_0 = 0$ is necessary to ensure that the single pulse phase current is not chopped, as shown in Fig. 5(c). This condition leads to α_z being equal to its analytical value, namely $\alpha_{Kom} = 0.65$, enabling accurate analysis of the optimal turn-OFF angle. Consequently, the analytical formula for α_{on_opt} under SPM can be expressed as

$$\alpha_{on\_opt} = -I_0 b'. \tag{29}$$

In summary, based on the SRM-QLNM, α_{on_opt} under CCM and SPM is solely dependent on I_0, with the analytical formula given by

$$\alpha_{on\_opt} = \begin{cases} -0.1 - I_0 b', & I_0 \le 1/(b - b') \\ -I_0 b', & I_0 > 1/(b - b'). \end{cases} \tag{30}$$

From the analytical formulas for the normalized excitation angles α_{on_opt} and α_{off_opt} in (27) and (30), it can be observed that as the SRG speed and load increase, I_0 increases, leading to a decrease in both α_{on_opt} and α_{off_opt}. The normalized conduction angle α_c is defined by (31), increases with I_0 until it reaches its maximum value of half a cycle, $3\tau/2$ [24]. At this point, the minimum value of α_{on_opt} is determined by α_{off_opt}. When I_0 is relatively small, the maximum constraint for α_{off_opt} is approximately 1 due to the minimal torque generated in the maximum inductance region. Therefore, the boundary constraint conditions for α_{on_opt} and α_{off_opt} are satisfied as expressed in (32).

$$\alpha_c = \alpha_{off} - \alpha_{on} = (\alpha_a + I_0 b')/1.35 \tag{31}$$

$$\begin{cases} \alpha_{on\_opt} \ge \alpha_{off\_opt} - 3\tau/2 \\ \alpha_{off\_opt} \le 1. \end{cases} \tag{32}$$

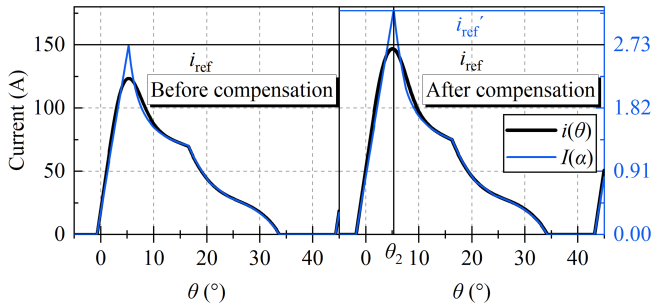

Fig. 11. Phase currents and their normalized values before and after reference current compensation.

TABLE III
CHARACTERISTIC PARAMETERS OF THE 8/6 FOUR-PHASE SRM

Parameters	Value
Stator pole arc angle θ_S (°)	20.5
Rotor pole arc angle θ_R (°)	23.5
the maximum inductance $L_{\max}$ (mH)	85
the minimum inductance $L_{\min}$ (mH)	8.5
Saturation current i_{sat} (A)	3.1

C. Reference Current Compensation

From Fig. 5(c), it can be observed that when $\alpha_0 = 0$, the peak phase current is less than the reference current due to the influence of fringing effect and back EMF in the low-inductance region. To address this issue, Ding et al. [25] analytically adjusted the θ_{on} from the perspective of magnetic flux to ensure that the peak phase current reaches the reference current at the inflection point θ_2. Under the condition that the reference current remains unchanged, the minimum inductance $L_{\min}$ is modified to the inductance value L_m corresponding to the position θ_2, as expressed in the following equation:

$$\theta_{\text{on\_opt}} = \theta_2 - \frac{\omega_r L_m i_{\text{ref}}}{U_{\text{dc}}}. \tag{33}$$

Since $L_{\min}$ serves as a characteristic parameter of the SRM-QLNM and is not easily altered, this study achieves the same objective through reference current compensation, as illustrated in Fig. 11. Based on (30), the implementation method involves initiating the current earlier by reducing θ_{on}. The relationship between the compensated reference current i'_{ref} and the original reference current i_{ref} is linear, as (34). It can be observed that the reference current compensation coefficient k remains constant, allowing for the estimation of coefficient k through a single experiment to ensure that the peak phase current reaches the reference value, thereby avoiding the need for measuring L_m.

$$i'_{\text{ref}} = i_{\text{ref}} L_m / L_{\min} = i_{\text{ref}} k. \tag{34}$$

D. Accuracy Verification of the Analytical Formulas for the Optimal Excitation Angles

To verify the accuracy and universality of the analytical formulas for the optimal excitation angles, both the 12/8 three-phase and 8/6 four-phase (characteristic parameters are provided in Table III) SRMs were employed. The optimal excitation angles were obtained by traversing θ_{on} and θ_{off} based on the multiobjective function value F_{obj} using the finite-element method (FEM) under different speeds n and reference currents i_{ref}. These results were then compared with those obtained through the analytical method.

Fig. 12(a) and (b) shows the comparison of $\theta_{\text{off\_opt}}$ obtained from the analytical method and FEM. In the FEM, θ_{on} was set according to (30) to ensure that the phase current peak reached the reference value, while θ_{off} was traversed with an accuracy of $0.5°$ to obtain $\theta_{\text{off\_opt}}$, as indicated by the black dots in Fig. 12. The 3-D surface and its projection in Fig. 12(a) and (b) represent the $\theta_{\text{off\_opt}}$ obtained through the analytical method. The results reveal that both SRMs exhibit high consistency in $\theta_{\text{off\_opt}}$ across all operating conditions for both methods. In addition, as n and i_{ref} increase, $\theta_{\text{off\_opt}}$ decreases, confirming the accuracy and universality of the analytical formula for $\theta_{\text{off\_opt}}$.

In SPM, $\theta_{\text{on\_opt}}$ obtained by compensating the reference current to i'_{ref}, enables the phase current to reach i_{ref} at θ_2 without chopping action, thus confirming the accuracy of the optimal conduction angle. Therefore, it is necessary to compare the analytical method and FEM results for $\theta_{\text{on\_opt}}$ in the CCM, as shown in Fig. 12(c) and (d). Since α_0 corresponds one-to-one with θ_{on}, which indicates the position where the phase current reaches the reference current, it is easier to analyze. In the FEM, α_0 was traversed with a precision of 0.02 under different n and i_{ref}, yielding $\theta_{\text{on\_opt}}$, represented by the black dots in Fig. 12. The 3-D surface and its projection in Fig. 12(c) and (d) illustrate $\theta_{\text{on\_opt}}$ obtained through the analytical method. The comparison shows that the consistency of $\theta_{\text{on\_opt}}$ obtained from both methods in the CCM is relatively low, attributed to the uncertainties introduced by the current chopping control, as detailed in Fig. 8. However, the error remains acceptable. As n and i_{ref} increase, $\theta_{\text{on\_opt}}$ decreases, further demonstrating the accuracy and universality of the analytical formula for $\theta_{\text{on\_opt}}$.

The optimal excitation angles analytical control block diagram based on SRM-QLNM is shown in Fig. 13. The speed loop outputs the reference current i_{ref} through a proportional-integral (PI) controller to control the phase current peak value. In SPM, due to the influence of back EMF, the phase current peak value cannot reach i_{ref}, necessitating compensation of the reference current to i'_{ref}. n and i'_{ref} are detected in real-time, and the SRM-QLNM converts them into the reference current normalized value I_0. $\alpha_{\text{on\_opt}}$ and $\alpha_{\text{off\_opt}}$ are obtained by substituting into (27) and (30), respectively. Finally, the actual values of the optimal excitation angles $\theta_{\text{on\_opt}}$ and $\theta_{\text{off\_opt}}$ are derived through denormalization, as (35). $\theta_{\text{on\_opt}}$, $\theta_{\text{off\_opt}}$, and i'_{ref} are processed and output as drive signals by the micro-control unit (MCU) to control the high-performance operation of the SRM.

$$\begin{cases} \theta_{\text{on\_opt}} = \alpha_{\text{on\_opt}} \theta_s + \theta_2 \\ \theta_{\text{off\_opt}} = \alpha_{\text{off\_opt}} \theta_s + \theta_2. \end{cases} \tag{35}$$

IV. EXPERIMENTAL VERIFICATION

To further validate the accuracy of the proposed SRM-QLNM and the analytical formulas of the optimal excitation angles, an experimental platform was established, as shown in Fig. 14. The

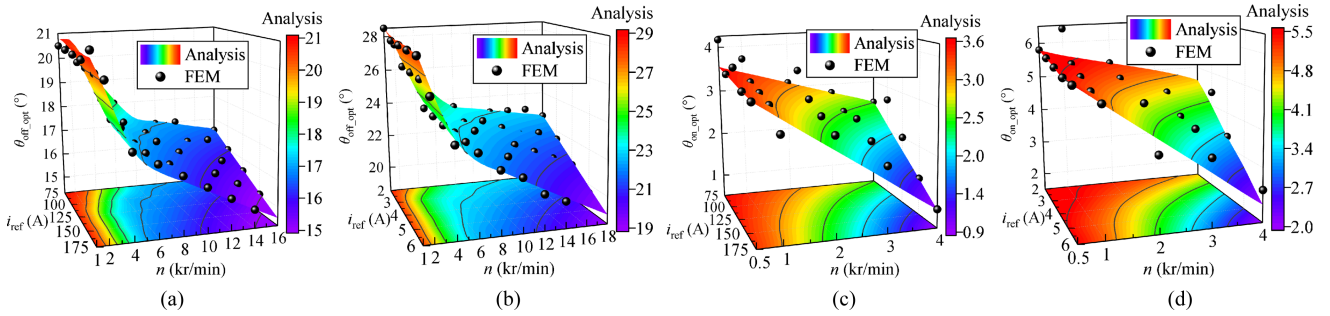

Fig. 12. Optimal excitation angles analytical method comparison with FEM. (a) θ_{off_opt} of 12/8 three-phase SRM. (b) θ_{off_opt} of 8/6 three-phase SRM. (c) θ_{on_opt} of 12/8 three-phase SRM. (d) θ_{on_opt} of 8/6 three-phase SRM.

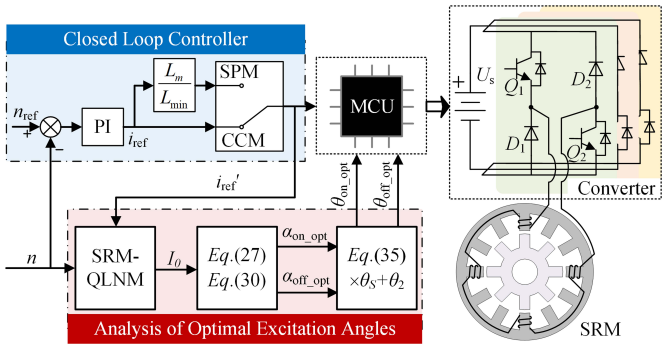

Fig. 13. Control block diagram for optimal excitation angles analysis based on the SRM-QLNM.

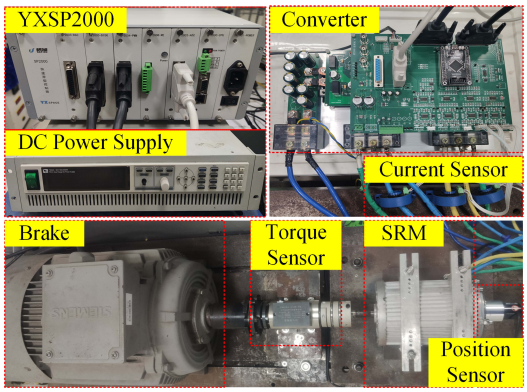

Fig. 14. Experiment platform.

TABLE IV
CHARACTERISTIC PARAMETERS OF THE 12/8 THREE-PHASE EXPERIMENTAL SRM

Parameters	Value
Stator pole arc angle θ_S (°)	15
Rotor pole arc angle θ_R (°)	19
The maximum inductance L_{max} (μH)	1700
The minimum inductance L_{min} (μH)	250
Saturation current i_{sat} (A)	46

characteristic parameters of the experimental 12/8 three-phase SRM are listed in Table IV, differing from those of the simulated SRM. An asymmetric half-bridge converter was employed with the dc bus voltage U_{dc} set to 48 V. The braking system utilized

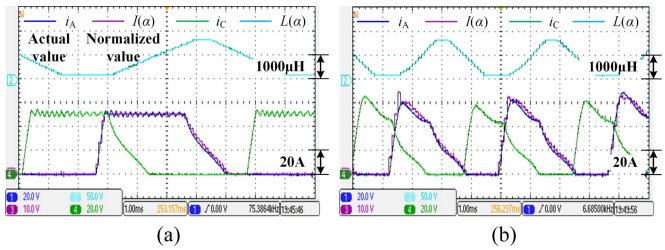

Fig. 15. Experimental waveforms of phase current and inductance. (a) CCM at 1000 r/min and 6.8 N · m. (b) SPM at 2000 r/min and 6.5 N · m.

an induction motor in generating mode. Phase current signals were collected via current sensors. The YXSP2000 controller generated drive signals based on commands at the control frequency of 10 kHz. These signals were processed by the complex programmable logic device (CPLD) to implement hardware current chopping.

Steady-state and dynamic experiments were conducted on the experimental platform. The steady-state experiments were divided into CCM and SPM, while the dynamic experiments included startup and load mutation conditions.

A. Steady-State Experiments

The experimental waveforms of Phase A and Phase C currents, i_A and i_C, the normalized current $I(\alpha)$ of Phase A, and the normalized inductance $L(\alpha)$, under the operating condition of SRM at a speed of 1000 r/min and a torque of 6.8 N · m are shown in Fig. 15(a). At this time, the operation mode is CCM, with $\theta_{on} = 1.8°$ and $\theta_{off} = 19.3°$.

The experimental waveforms of i_A, i_C, $I(\alpha)$, and $L(\alpha)$, under the operating condition of the SRM at a speed of 2000 r/min and a torque of 6.5 N · m are shown in Fig. 15(b). At this time, the operation mode is SPM, with $\theta_{on} = 0.9°$ and $\theta_{off} = 17°$.

By comparing Fig. 15(a) and (b), it is observed that the consistency between i_A and $I(\alpha)$ is high, confirming the accuracy of SRM-QLNM under both CCM and SPM. The position where i_A first reaches the reference current i_{ref} (50 A) occurs at 4° under CCM and at 5.5° under SPM, aligning with the definition of the optimal turn-ON angle. In both cases, $\alpha_{Kom} = 0.65$, confirming the accuracy of the optimal excitation angles. Notably, under SPM, to ensure that the peak value of i_A reaches $i_{ref} = 60$ A, the

TABLE V
EXPERIMENTAL RESULTS COMPARISON

Mode	Method	$\theta_{on}(^\circ)$	$\theta_{off}(^\circ)$	$\eta(\%)$	$T_{avg}(\mathrm{N\cdot m})$	$\Delta T(\%)$	F_{obj}
CCM	Proposed	1.8	19.3	84	6.8	26	0.6
	[25]	3.1	15.6	86	5.8	104	0.4
SPM	Proposed	0.9	17	90	6.5	75	0.6
	[25]	0.9	13.4	91	5.3	148	0.4

reference current compensation coefficient is set to $k = 1.15$, demonstrating the effectiveness of the reference current compensation.

The experimental results based on the excitation angles obtained from the proposed analytical formulas and the latest study [25] are compared in Table V. In CCM, $n = 1000\,\mathrm{r/min}$ and $i_{ref} = 50\,\mathrm{A}$; in SPM, $n = 2000\,\mathrm{r/min}$ and $i_{ref} = 60\,\mathrm{A}$. First, the turn- ON angle is analyzed. In CCM, Ding et al. [25] set θ_{on} such that $\alpha_0 = 0$, whereas proposed method sets $\alpha_0 = -0.1$, as shown in (30). Therefore, compared to [25], θ_{on} obtained by proposed method is smaller. According to Fig. 7, appropriately reducing θ_{on} can, on one hand, utilize the transition region between the minimum inductance and the rising region to generate torque, thereby increasing T_{avg}. On the other hand, it can raise the composite torque valley value, thus suppressing ΔT. Since the rate of change of inductance in this transition region is small, resulting in lower torque generation efficiency, the motor efficiency is slightly lower compared to [25]. In SPM, θ_{on} obtained by the proposed method is the same as that in [25], with both being 0.9° as shown in Table V. This is because both methods set $\alpha_0 = 0$ to calculate θ_{on}.

Next, the turn- OFF angle is analyzed. The proposed method defines θ_{off_opt} to achieve $\alpha_{Kom} = 0.65$, while in [25], the conduction width is fixed at 12.5°. Therefore, compared to [25], θ_{off} obtained by the proposed method is larger, as shown in Table V. As shown in Fig. 6, a smaller θ_{off} corresponds to a smaller α_{Kom}. Therefore, θ_{off} obtained by the proposed method results in a larger average torque and smaller torque ripple compared to [25], with efficiency not being significantly lower, and possibly even higher.

According to Table V, while the proposed method exhibits slightly lower efficiency η than [25] in both CCM and SPM, it achieves significantly higher T_{avg} and reduced ΔT, leading to a greater multiobjective function value F_{obj}. Under CCM, η decreases by 2%, while T_{avg} increases by 17% and ΔT decreases by 78% . Under SPM, η decreases by 1%, while T_{avg} increases by 23% and ΔT decreases by 73% . The comparison of the electromagnetic torque waveforms obtained using the proposed method in CCM and SPM with those in [25] as shown in Fig. 16(a) and (b), respectively. These results further confirm the effectiveness of the optimal excitation angles derived from SRM-QLNM.

B. Dynamic Experiments

As shown in Fig. 17(a), the experimental waveforms during the startup process with a load torque of $6.5\,\mathrm{N\cdot m}$ and motor speed increasing from 0 to $2000\,\mathrm{r/min}$ are presented. From

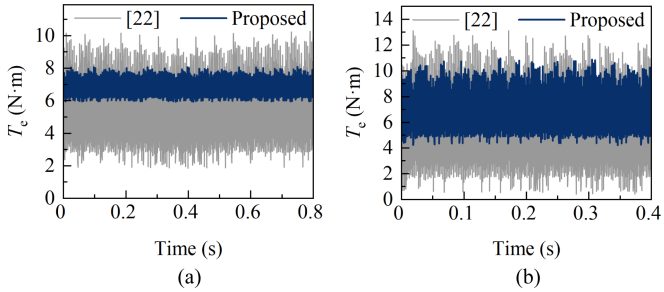

Fig. 16. Experimental waveforms comparing the electromagnetic torque. (a) CCM. (b) SPM.

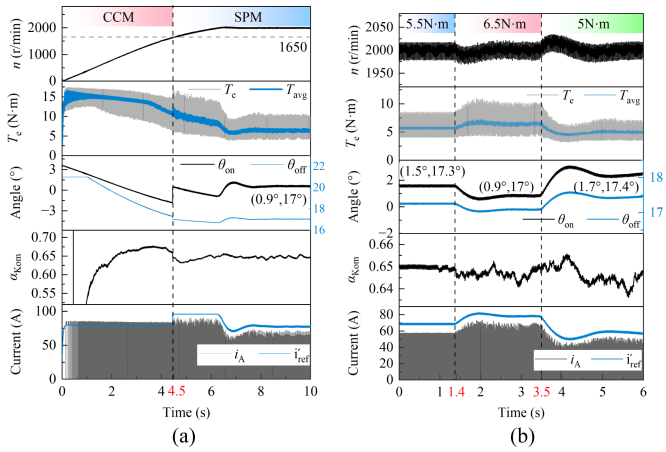

Fig. 17. Dynamic experimental waveforms. (a) Starup process. (b) Load mutation.

top to bottom, the waveforms include speed n, electromagnetic torque T_e, and average torque T_{avg}, turn-ON angle θ_{on} and turn-OFF angle θ_{off}, turn-OFF ratio α_{Kom}, phase current i_A, and compensated reference current i'_{ref}. The PI output saturation limit and integral saturation limit are both set to 80 A, with antiwindup integral control applied.

During startup, operation below $1650\,\mathrm{r/min}$ is in CCM, transitioning to SPM above $1650\,\mathrm{r/min}$. After stabilizing at $2000\,\mathrm{r/min}$, the average torque equals the load torque, achieving dynamic equilibrium. Both θ_{on} and θ_{off} are calculated in real-time, adapting to variations in speed and load, and eventually stabilize at $(-1.2^\circ, 17^\circ)$. α_{Kom} remains approximately constant at 0.65, validating the accuracy of the real-time calculation of the optimal excitation angles.

As shown in Fig. 17(b), the experimental waveforms depict the process where the motor speed stabilizes at $2000\,\mathrm{r/min}$, and the load torque increases abruptly from 5.5 to $6.5\,\mathrm{N\cdot m}$ at 1.4 s, and then, decreases abruptly to $5\,\mathrm{N\cdot m}$ at 3.5 s. Corresponding to Fig. 17(b), n will drop when the load torque increases, otherwise, n will rise. Using the analytical method, both θ_{on} and θ_{off} decrease with increasing load, ensuring that α_{Kom} remains approximately stable at 0.65. The excitation angles for three different loads are indicated in Fig. 17(b). Compared to θ_{off}, θ_{on} exhibits more significant variation. The accuracy and feasibility

of the optimal excitation angles analysis were validated through dynamic experiments.

V. Conclusion

To address the existing issues of complex structure, poor generality, and the inability to simultaneously optimize the torque per ampere, average torque, and torque ripple in the analytical formulas of the optimal excitation angles for the SRM, SRM-QLNM is proposed in this article. By normalizing various parameters, the challenges of SRM's model complexity and generality in the optimal excitation angle analytical formulas are resolved. A multiobjective function is constructed to summarize the law of the optimal excitation angles and derive their analytical formulas. Considering the fringing effect and back EMF in the low-inductance region, a compensation for the reference current in the SPM is implemented to ensure that the phase current peak value reaches the reference value. Through theoretical analysis, simulations, and experimental validation, the following conclusions are drawn:

1) To simplify the phase current analytical formula, four original basic values are defined based on the traditional SRM-QLM by relocating the coordinate origin to θ_2, as (8). Accordingly, the parameters are normalized to obtain the SRM-QLNM. The analytical formulas of the optimal excitation angles derived from SRM-QLNM are structurally simple and possess generality.
2) The optimal excitation angles for maximizing the multiobjective function value are derived by setting $\alpha_{\text{Kom}} = 0.65$ for $\alpha_{\text{off\_opt}}$ in (27) and selecting $\alpha_0 = -0.1$ under CCM and $\alpha_0 = 0$ under SPM for $\alpha_{\text{on\_opt}}$ in (30). Both expressions depend solely on I_0. Finally, through inverse normalization, the optimal excitation angles $\theta_{\text{on\_opt}}$ and $\theta_{\text{off\_opt}}$ are obtained. Compared to [22], a significant improvement in T_{avg} and ΔT was achieved at the cost of a slight reduction in η, facilitating an effective enhancement of the overall performance of SRM across the entire torque–speed range.

References

[1] Y. Hu, W. Ding, T. Wang, S. Li, S. Yang, and Z. Yin, "Investigation on a multimode switched reluctance motor: Design, optimization, electromagnetic analysis, and experiment," *IEEE Trans. Ind. Electron.*, vol. 64, no. 12, pp. 9886–9895, Dec. 2017.

[2] L. Ge, J. Zhong, J. Huang, N. Jiao, S. Song, and R. W. De Doncker, "A novel model predictive torque control of SRMs with low measurement effort," *IEEE Trans. Ind. Electron.*, vol. 70, no. 4, pp. 3561–3570, Apr. 2023.

[3] L. Ge et al., "Advanced technology of switched reluctance machines in more electric aircraft: A review," *IEEE Trans. Power Electron.*, vol. 40, no. 1, pp. 195–216, Jan. 2025.

[4] L. Al Quraan and L. Szamel, "Torque ripple reduction of switched reluctance motor using direct instantaneous torque control and adaptive turn-on technique for electric vehicle applications," *IET Electric Power Appl.*, vol. 17, no. 12, pp. 1502–1514, Dec. 2023.

[5] F. Al-Amyal, M. Hamouda, and L. Számel, "Performance improvement based on adaptive commutation strategy for switched reluctance motors using direct torque control," *Alexandria Eng. J.*, vol. 61, no. 11, pp. 9219–9233, Nov. 2022.

[6] H. Cheng, H. Chen, and Z. Yang, "Average torque control of switched reluctance machine drives for electric vehicles," *IET Electric Power Appl.*, vol. 9, no. 7, pp. 459–468, Aug. 2015.

[7] L. Ge, J. Guo, C. Gong, G. Zhang, X. Ding, and S. Song, "Model predictive torque control of switched reluctance machines with torque sharing function and PWM control signals based on linear polynomial fitting," *IEEE Trans. Power Electron.*, vol. 40, no. 1, pp. 40–45, Jan. 2025.

[8] W. Ding, G. Liu, and P. Li, "A hybrid control strategy of hybrid-excitation switched reluctance motor for torque ripple reduction and constant power extension," *IEEE Trans. Ind. Electron.*, vol. 67, no. 1, pp. 38–48, Jan. 2020.

[9] T. Husain, A. Elrayyah, Y. Sozer, and I. Husain, "Flux-weakening control of switched reluctance machines in rotating reference frame," *IEEE Trans. Ind. Appl.*, vol. 52, no. 1, pp. 267–277, Jan./Feb. 2016.

[10] T. Husain, A. Elrayyah, Y. Sozer, and I. Husain, "Dq control of switched reluctance machines," in *Proc. IEEE 28th Annu. Appl. Power Electron. Conf. Expo.*, Mar. 2013, pp. 1537–1544.

[11] T. Husain, A. Elrayyah, Y. Sozer, and I. Husain, "Unified control for switched reluctance motors for wide speed operation," *IEEE Trans. Ind. Electron.*, vol. 66, no. 5, pp. 3401–3411, May. 2019.

[12] M. Hamouda, A. Abdel Menaem, H. Rezk, M. N. Ibrahim, and L. Számel, "Comparative evaluation for an improved direct instantaneous torque control strategy of switched reluctance motor drives for electric vehicles," *Mathematics*, vol. 9, no. 4, Feb. 2021, Art. no. 302.

[13] L. Al Quraan, L. Szamel, and M. Hamouda, "Optimum switching angles control of SRM for electric vehicle applications," *Periodica Polytechnica Elect. Eng. Comput. Sci.*, vol. 65, no. 4, pp. 394–403, Oct. 2021.

[14] M. M. Islam, M. K. M. Bin Azam, A. Siddiquee, and Y. Sozer, "Multiobjective optimization of the control parameters of SRM incorporating core loss estimation," in *Proc. IEEE Energy Convers. Congr. Expo.*, Nashville, TN, USA, Oct. 2023, pp. 5055–5059.

[15] A. L. Saleh, F. Al-Amyal, and L. Számel, "An enhanced current chopping control strategy for SRM drives using harris hawks optimization algorithm," *ISA Trans.*, vol. 150, pp. 338–358, Jul. 2024.

[16] X. Xue et al., "Optimal control method of motoring operation for SRM drives in electric vehicles," *IEEE Trans. Veh. Technol.*, vol. 59, no. 3, pp. 1191–1204, Mar. 2010.

[17] J. W. Jiang, F. Peng, B. Bilgin, and A. Emadi, "Optimisation-based procedure for characterising switched reluctance motors," *IET Electric Power Appl.*, vol. 11, no. 8, pp. 1366–1375, Sep. 2017.

[18] J. Xiu, S. Wang, and Y. Xiu, "Optimum firing angles control for switched reluctance motor based on IPSO at steady state," *IEEE Trans. Energy Convers.*, vol. 38, no. 2, pp. 780–788, Jun. 2023.

[19] Y. Sozer and D. Torrey, "Optimal turn-off angle control in the face of automatic turn-on angle control for switched-reluctance motors," *IET Electric Power Appl.*, vol. 1, no. 3, pp. 395–401, May. 2007.

[20] Y. Sozer, D. Torrey, and E. Mese, "Automatic control of excitation parameters for switched-reluctance motor drives," *IEEE Trans. Power Electron.*, vol. 18, no. 2, pp. 594–603, Mar. 2003.

[21] S. Song, G. Fang, R. Hei, J. Jiang, R. Ma, and W. Liu, "Torque ripple and efficiency online optimization of switched reluctance machine based on torque per ampere characteristics," *IEEE Trans. Power Electron.*, vol. 35, no. 9, pp. 9608–9616, Sep. 2020.

[22] C. Mademlis and I. Kioskeridis, "Performance optimization in switched reluctance motor drives with online commutation angle control," *IEEE Trans. Energy Convers.*, vol. 18, no. 3, pp. 448–457, Sep. 2003.

[23] Y. Z. Xu, R. Zhong, L. Chen, and S. L. Lu, "Analytical method to optimise turn-on angle and turn-off angle for switched reluctance motor drives," *IET Electric Power Appl.*, vol. 6, no. 9, pp. 593–603, Nov. 2012.

[24] R. Rocca, F. G. Capponi, S. Papadopoulos, G. De Donato, M. Rashed, and M. Galea, "Optimal advance angle for aided maximum-speed-node design of switched reluctance machines," *IEEE Trans. Energy Convers.*, vol. 35, no. 2, pp. 775–785, Jun. 2020.

[25] S. Ding, X. Huang, J. Hang, and W. Li, "Improved efficiency optimization control of SRM based on redefined optimal turn-on angle and its corresponding analytical formula," *IEEE Trans. Power Electron.*, vol. 39, no. 12, pp. 16508–16520, Dec. 2024.

[26] I. Kioskeridis and C. Mademlis, "Maximum efficiency in single-pulse controlled switched reluctance motor drives," *IEEE Trans. Energy Convers.*, vol. 20, no. 4, pp. 809–817, Dec. 2005.

[27] A. Shahabi, A. Rashidi, M. Afshoon, and S. M. Saghaian Nejad, "Commutation angles adjustment in SRM drives to reduce torque ripple below the motor base speed," *Turkish J. Elect. Eng. Comput. Sci.*, vol. 24, pp. 669–682, 2016.

[28] F. Al-Amyal and L. Számel, "Analytical approach for the turn-off angle in switched reluctance motors," in *Proc. 6th Int. Congr. Inf. Commun. Technol.*, X.-S. Yang, S. Sherratt, N. Dey, and A. Joshi, Eds., vol. 217. Singapore: Springer 2022, pp. 685–696.

[29] M. Hamouda and L. Számel, "A new technique for optimum excitation of switched reluctance motor drives over a wide speed range," *Turkish J. Elect. Eng. Comput. Sci.*, vol. 26, no. 5, pp. 2753–2767, Sep. 2018.
[30] Z. Chai, C. Liu, T. Wang, and X. Zhu, "Comprehensive performance improvement of SRG by Turn-ON angle optimization using linear normalized model," *IEEE Trans. Power Electron.*, vol. 39, no. 5, pp. 6327–6337, May. 2024.
[31] T. J. E. Miller, "Converter volt-ampere requirements of the switched reluctance motor drive," *IEEE Trans. Energy Convers.*, vol. IA-21, no. 5, pp. 1136–1144, Sep. 1985.
[32] S. Bolognani and M. Zigliotto, "Fuzzy logic control of a switched reluctance motor drive," *IEEE Trans. Ind. Appl.*, vol. 32, no. 5, pp. 1063–1068, Sep./Oct. 1996.
[33] R. Orthmann and H. Schoner, "Turn-off angle control of switched reluctance motors for optimum torque output," in *Proc. 5th Eur. Conf. Power Electron. Appl.*, Sep. 1993, pp. 20–25.

Zhiyuan Chai (Graduate Student Member, IEEE) received the B.S. and M.S. degrees in electrical engineering, in 2020 and 2023, respectively from the Nanjing University of Aeronautics and Astronautics, Nanjing, China, where he is currently working toward the Ph.D. degree in electrical engineering.

His research interests include high-efficiency switched reluctance machine drive systems for automotive, aerospace applications, and renewable energy, especially the starter/generator systems.

Yuefei Zuo (Member, IEEE) received the B.Eng. degree in electrical engineering and automation and the Ph.D. degrees in power electronics and electrical drives both from the Nanjing University of Aeronautics and Astronautics, Nanjing, China, in 2010 and 2016, respectively.

From July 2016 to February 2019, he was a Lecturer with the School of Electrical and Information Engineering, Jiangsu University, Zhenjiang, China. In March 2019, he joined the School of Electrical and Electronic Engineering, Nanyang Technological University, Singapore, as a Research Fellow, and was promoted to a Senior Research Fellow in July 2022. In Aprril 2023, he joined the Department of Aeronautical and Automotive Engineering, Loughborough University, Loughborough, U.K., as a Research Associate. He is currently a Full Professor with the College of Automation Engineering, Nanjing University of Aeronautics and Astronautics. His research interests include power electronics, electric machines and drives, active disturbance rejection control, model predictive control, and artificial intelligence (AI).

Shushu Zhu received the B.Eng., M.S., and Ph.D. degrees in electrical engineering from the Nanjing University of Aeronautics and Astronautics, Nanjing, China, in 2009, 2012, and 2017, respectively.

From 2016 to 2017, she was a Visiting Scholar with Electrical Energy Management Group, Department of Electrical and Electronic Engineering, University of Bristol, Bristol, U.K. She is currently a Professor with the College of Automation Engineering, Nanjing University of Aeronautics and Astronautics. Her research interests include renewable power systems and electrical machine driving systems.

Minjun Guan received the B.Eng., M.Eng., and the Ph.D. degrees in electrical engineering from the Nanjing University of Aeronautics and Astronautics, Nanjing, China, in 2011, 2014, and 2020, respectively.

She is currently a Lecturer with the College of Mechanical and Electrical Engineering, Jinling Institute of Technology, Nanjing. Her research interests include high-efficiency switched reluctance motor drive systems for automotive, renewable energy, and household appliances, especially the research of novel power converter of multiphase SRMs.

Yao Sun received the B.S. degree in electrical engineering in 2021 from the Nanjing University of Aeronautics and Astronautics, Nanjing, China, where she is currently working toward the Ph.D. degree in electrical engineering.

Her main research interests include the design and optimization of the doubly salient electric machine for aircraft power.

Wen Li received the bachelor's degree in aircraft power engineering, in 2020, from the Nanjing University of Aeronautics and Astronautics, Nanjing, China, where she is currently working toward the Ph.D. degree in aeronautical and astronautical science and technology.

Her research interests include heat and mass transfer.

Chuang Liu was born in Anhui, China, in 1973. He received the B.S. degree in electrical engineering from Yanshan University, Qinhuangdao, China, in 1994, and the M.S. and Ph.D. degrees in electrical engineering from the Nanjing University of Aeronautics and Astronautics, Nanjing, China, in 1997 and 2000, respectively.

In 2000, he was a Postdoctoral Researcher with the Nanjing University of Aeronautics and Astronautics, where he joined the Department of Electrical Engineering, in 2002. He has been a Professor with the Department of Electrical Engineering, College of Automation Engineering, Nanjing University of Aeronautics and Astronautics, since 2008. His research interests include the permanent-magnet synchronous motors and switched reluctance motors for automotive, renewable energy, and aerospace applications.